

See discussions, stats, and author profiles for this publication at: <https://www.researchgate.net/publication/283650238>

Effect of Wing Kinematics Modulation on Aerodynamic Force Generation in Hovering Insect-mimicking Flapping-wing Micro Air Vehicle

Article in *Journal of Bionic Engineering* · October 2015

DOI: 10.1016/S1672-6529(14)60144-X

CITATIONS

17

READS

212

4 authors:



Hoang Vu Phan

École Polytechnique Fédérale de Lausanne

46 PUBLICATIONS 585 CITATIONS

[SEE PROFILE](#)



Tri Truong

Ho Chi Minh City University of Technology and Education (HCMUTE), Ho Chi Minh,...

2 PUBLICATIONS 17 CITATIONS

[SEE PROFILE](#)



Au Thi Kim Loan

Konkuk University

18 PUBLICATIONS 144 CITATIONS

[SEE PROFILE](#)



Hoon Cheol Park

Konkuk University

259 PUBLICATIONS 3,900 CITATIONS

[SEE PROFILE](#)

Some of the authors of this publication are also working on these related projects:



GUEST EDITOR for "APPLIED SCIENCES": Special issue on "BIOINSPIRED FLIGHT" [View project](#)



Flapping Type Tidal Energy Harvester [View project](#)

Effect of Wing Kinematics Modulation on Aerodynamic Force Generation in Hovering Insect-mimicking Flapping-wing Micro Air Vehicle

Hoang Vu Phan^{1,2,3}, Quang Tri Truong⁴, Thi Kim Loan Au^{1,2,3}, Hoon Cheol Park^{1,2,3}

1. Artificial Muscle Research Center, Konkuk University, Seoul 143-701, South Korea

2. National Research Laboratory for Biomimetics and Intelligent Microsystems, Konkuk University, Seoul 143-701, South Korea

3. Department of Advanced Technology Fusion, Konkuk University, Seoul 143-701, South Korea

4. Laboratory of Applied Mechanics, Faculty of Applied Science, Ho Chi Minh City University of Technology, Ho Chi Minh 740-128, Vietnam

Abstract

We investigated the effect of wing kinematics modulation, which was achieved by adjusting the location of trailing-edge constraint at the wing-root, i.e., by adjusting the wing-root offset, on the generation of aerodynamic forces in a hovering insect-mimicking Flapping-Wing Micro Air Vehicle (FW-MAV) by numerical and experimental studies. Three-dimensional wing kinematics measured using three synchronized high-speed cameras revealed a clear difference in the wing rotation angle of a wing section for different wing-root offsets. The extrapolated wing kinematics were in good agreement with the measured ones for various wing-root offsets. The Unsteady Blade Element Theory (UBET) was used to estimate the forces generated by the flapping wings and validated by comparison with results of measurements performed using a load cell. Although the thrust produced by a flapping wing with a wing-root offset of $0.20 \bar{c}$ was about 4% less, its force-to-input-power ratio was about 30% and 10% higher than those with the offsets of $0.10 \bar{c}$ and $0.15 \bar{c}$, respectively. This result could be explained by analyzing the effective Angle of Attack (AoA) and the force components computed by the UBET. Thus, a flapping wing with a wing-root offset of $0.20 \bar{c}$ can be regarded as an optimal twist configuration for the development of the FW-MAV.

Keywords: wing kinematics, flapping-wing MAV, biomimetics, beetle-mimicking, insect flight, linear extrapolation

Copyright © 2015, Jilin University. Published by Elsevier Limited and Science Press. All rights reserved.

doi: 10.1016/S1672-6529(14)60144-X

1 Introduction

In nature, insects show remarkable flight performance, e.g., high maneuverability at low flight speeds in confined spaces, capability of stable hovering, and high energy efficiency. Many robotics and aeronautical engineers have drawn inspiration from the flight of insects because it has possible applications to the development of Flapping-Wing Micro Air Vehicles (FW-MAVs)^[1–4]. Numerous studies employing both computational and experimental methods have been conducted on flapping insect wings with the aim of revealing the mechanism of their unsteady aerodynamics^[5–10]. The results of such studies have elucidated the fundamental principles of generation of unsteady aero-

dynamic forces in insect flight, which is not satisfactorily explained by conventional wing theories based on steady aerodynamics, such as the clap and fling, leading-edge-vortex generation, delayed stall, wake capture, and rotational force.

Nevertheless, most of these studies were conducted using the rigid flat-plate wing. Meanwhile, studies on wing kinematics indicated that most insect wings, including those of hoverflies^[11], beetles^[12–14], bumblebees^[15], hawkmoths^[16], and locusts^[17,18], actively deform during the flapping motion. The effects of wing deformation, i.e., chordwise camber and spanwise twist, on aerodynamic force generation have been investigated extensively. Du and Sun^[19] conducted a computational study by using the wing kinematics measurements of

Walker *et al.*^[11] in order to investigate the effects of the camber deformation and twist deformation on aerodynamic forces in hovering hoverflies. The considered flapping frequencies and flapping amplitudes ranged from 150 Hz to 180 Hz and 70° to 130°, respectively. Their model showed that the cambered wing generated higher lift than the rigid flat-plate wing, whereas a spanwise twist wing played a significant role in reducing only the required power. However, Nakata and Liu^[16], who constructed a computational Fluid-Structure Interaction (FSI) model based on the wing kinematics of a hovering hawkmoth, found that the flexible wing, in which camber was not considered significantly, was beneficial from the viewpoints of generation of aerodynamic forces and efficiency during hovering. Moreover, Truong *et al.*^[20] applied the three-dimensional (3D) wing kinematics of artificial wings of an insect-mimicking flapping-wing system, which mimics the hovering flight of a real beetle, to an Unsteady BladeElement Theory (UBET) model and revealed that a passive wing twist improves the average vertical force by about 9.5% while consuming less power than the rigid wing. Thus, wing deformation indeed plays an important role in maximizing the generation of aerodynamic forces and reducing the required power for hovering insects and robotic flapping-wing systems.

Such active modulation of wing kinematics in insects may be not available in man-made fliers, because it requires much endeavor to mimic. Instead, several FW-MAVs using passive wing twist mechanism have been developed for mimicking the flight of hummingbirds or hovering insects^[2,21,22]. Here, it is noteworthy that the flight performance of hummingbirds is similar to that of hovering insects. The tailless Nano Hummingbird developed by Keenoon *et al.*^[2] is a unique and first-ever system that was able to successfully demonstrate a variety of controlled maneuvering flights by just flapping its wings. In an attempt to exploit the benefits of insect flight, we have also been developing an insect-mimicking FW-MAV, which mimics the flight of a beetle, *Allomyrina dichotoma*. Our FW-MAV, with a wing area of 10 cm², can generate a thrust of about 10 g at a flapping angle of 140° and flapping frequency of about 40 Hz, which are close to the natural values of a beetle^[20,23]. A passive wing twist mechanism, which was demonstrated to be beneficial for the generation of larger forces^[20], was implemented in the system. The system

could vertically take off with an integrated battery and electronic circuit^[23].

It is obvious that for flight, a hovering FW-MAV should be designed to produce enough vertical force to sustain its body weight. A larger vertical force can be obtained by increasing the flapping stroke amplitude and wing beat frequency^[24]. Some studies found that hummingbirds also maximized the vertical force by enhancing the flapping stroke amplitude and wing beat frequency^[25,26]. Another important parameter that can be considered to maximize the vertical aerodynamic force is the wing rotation angle or Angle of Attack (AoA). Most studies for measuring the lift and drag coefficients as a function of AoA were conducted under the assumption of a rigid wing^[6,8,27–29]. Although wing twist can be beneficial for the generation of larger forces, precise determination of the AoA is a nontrivial task, since the wing rotation angle varies from the root to the tip during flapping motion. Therefore, finding an optimal wing rotation angle in order to effectively improve the vertical force is an important task from the viewpoint of developing a hovering insect-mimicking FW-MAV using passive wing twist.

In the present work, we investigated how passive wing kinematics modulation affects the vertical force generation characteristics in terms of magnitude and efficiency, by adjusting the location of the trailing-edge constraint at the wing root, i.e., by adjusting the wing-root offset. The wing-root offset can be regarded as margin of wing membrane when it is installed to the flapping-wing mechanism. Changing the offset is expected to modify the passive wing twist and eventually change the AoA of wing sections along the wingspan during flapping motion. We examined five cases of wing kinematics corresponding to five different wing-root offsets. A flapping-wing mechanism that is capable of smooth beating with high flapping amplitude was used for the test. This mechanism employed a combination of the slider-crank and pulley-string mechanisms to transfer the rotary motion of the motor to the flapping motions of the wings. We first measured the 3D wing kinematics, i.e., flapping angle and wing rotation angle, by using three high-speed cameras synchronized at 2000 fps. Then, we applied the measured wing kinematics to the UBET to estimate the forces generated by the wings at each wing-root offset. We validated the estimated data by comparing them with experimental data obtained

from measurements performed using a load cell. We then conducted a numerical study to explain why a specific wing-root offset could provide larger vertical force and to evaluate the contribution of each force component to the resultant vertical force. In addition, by using linear extrapolation and interpolation techniques, we also verified how the passive wing twist mechanism modulates the wing rotation angle corresponding to the change in the wing-root offset.

2 Design of hovering FW-MAV

2.1 Flapping mechanism for large flapping angle

The design of the flapping mechanism was based on a combination of the slider-crank and pulley-string mechanisms. Figs. 1a and 1b show the schematic of the flapping mechanism, and Fig. 1c shows the model of the mechanism constructed using CAD software. The rotational motion (ϕ) of the crank (d) is converted to the linear oscillation of the horizontal slider along the vertical column, which is connected to the couplers (O_1O_2); the linear motion is then transformed to the flapping motion (β) of the linkage O_2O_3 . This linkage is rigidly glued to the large pulley, which in turn is connected to the small pulley through a string. This pulley mechanism amplifies the flapping motion (β) to a larger flapping motion of the output link (ψ) owing to the difference in the radii of the two pulleys.

Through vector analysis, the relationship of the

linkage in Fig. 1a can be expressed in the x and y directions as

$$O_0O_3 = d \sin \phi + l \cos \gamma + O_1O_2 \cos \alpha - O_2O_3 \sin \beta, \quad (1)$$

$$O_1O_2 \sin \alpha = O_2O_3 \cos \beta, \quad (2)$$

$$d \cos \phi = l \sin \gamma, \quad (3)$$

where d and l are the lengths of the crank and the connecting rod, respectively. Eqs. (1–3) can be reduced to

$$\sin \beta = \frac{O_1O_2^2 - O_2O_3^2 - (O_0O_3 - d \sin \phi - l \cos \gamma)^2}{2O_2O_3(O_0O_3 - d \sin \phi - l \cos \gamma)}, \quad (4)$$

$$d = \frac{l \sin \gamma}{\cos \phi}. \quad (5)$$

The relationship between the flapping angles ψ and β can be determined by

$$\psi = \frac{r_1}{r_2} \beta. \quad (6)$$

When the crank rotates by an angle ϕ from $-\pi/2$ to $\pi/2$, the linkage O_2O_3 sweeps from β_{\min} to β_{\max} as shown in Fig. 1b. Once the flapping angle ψ is chosen, β is calculated for given r_1 and r_2 . Then, the lengths of the linkages can be determined as

$$d = \frac{O_2O_3(O_0O_3 - l)(\sin \beta_{\max} - \sin \beta_{\min})}{O_2O_3(\sin \beta_{\max} + \sin \beta_{\min}) + 2(O_0O_3 - l)}, \quad (7)$$

$$O_1O_2 = \sqrt{2O_2O_3(O_0O_3 - d - l) \sin \beta_{\max} + O_2O_3^2 + (O_0O_3 - d - l)^2}. \quad (8)$$

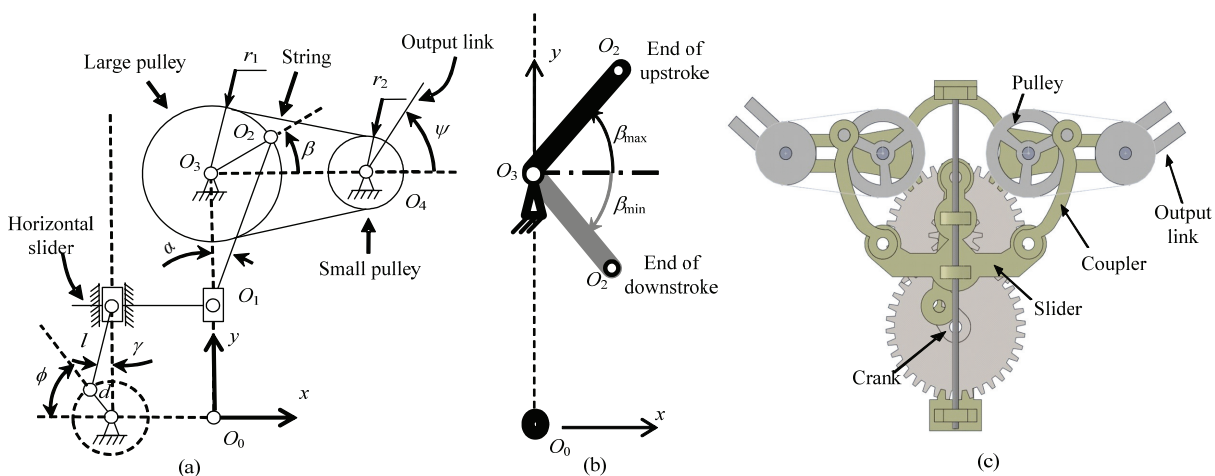


Fig. 1 (a) Schematic illustration of flapping mechanism, (b) definition of angle β when the crank rotates from $-\pi/2$ to $\pi/2$, and (c) front view of CAD model.

For fabricating the mechanism, we first designed the virtual parts and assembled them using 3D CAD software, as shown in Fig. 1c, to ensure successful assembly after fabrication of the actual parts. Fig. 2a shows the time history of the flapping angle designed from the virtual CAD model. Subsequently, we used 0.8-mm-thick glass/epoxy panels to fabricate all linkages and supporting frames. The parts were built according to the CAD design by using a computer numerical control (CNC) machine (MM-300S, resolution 10 μm , MANIX, Korea) and then assembled manually as shown in Fig. 2b. The gear ratio of the flapping mechanism was 12:1.

2.2 Design of wing shape and wing-root offset

The wings are attached to the output links of the flapping mechanism to generate aerodynamic forces during flapping motion. To produce flapping motion at a higher frequency, the wings should be designed to be as light as possible but still stiff enough to carry the load on the wings. In our work, the veins and membrane of the wings were made of carbon/epoxy strips and 20- μm -thin polyethylene terephthalate (PET), respectively, as shown in Fig. 3. The leading edge of the wing was made of 50-mm-length, 0.6-mm-thick, 2-mm-wide carbon/epoxy strips, and other veins were made of 0.2-mm-thick, 0.8-mm-wide carbon/epoxy strips. All veins were vacuum-bagged and cured in an oven at an appropriate temperature^[30] before being glued to the wing membrane. The total weight of each wing after assembly was about 0.1 g. Details of the fabrication of the artificial wings and the constraints of the trailing edge near the wing roots can be found elsewhere^[20,23,31].

When the wings were installed in the flapping mechanism, the wing roots were connected to the trailing-edge connector, as shown in Fig. 4. With this configuration, the flapping-wing system could produce passive wing twist during the flapping motion, which was previously proved to increase thrust significantly^[20]. Changing the wing root position along the trailing-edge connector can modify the passive wing twist, resulting in modification in wing kinematics, and eventually affect the aerodynamic performance of the wing during flapping motion.

As shown in Fig. 4, the root of the right wing was placed at the reference location, where the wing membrane has no curvature or camber. Holes were drilled

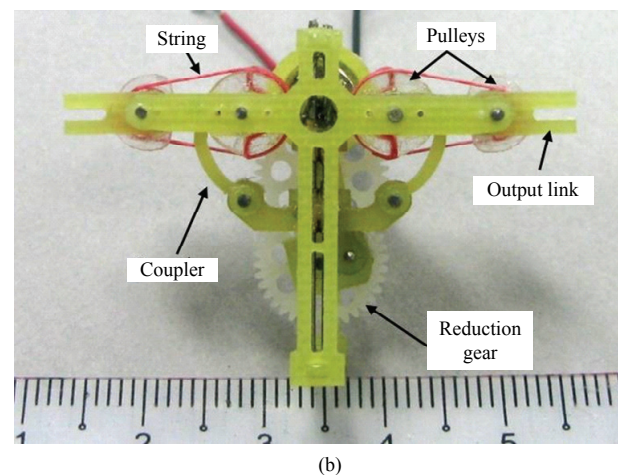
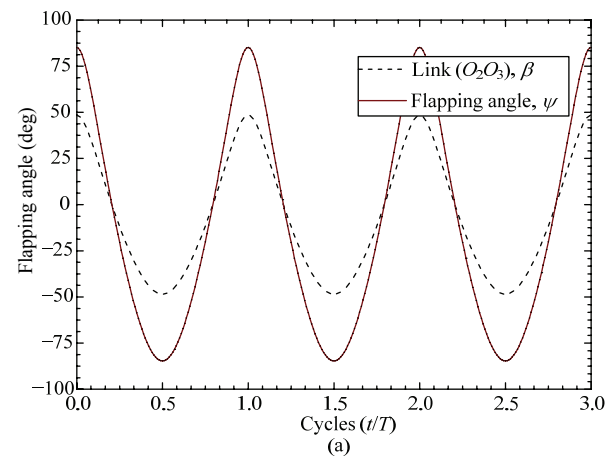


Fig. 2 (a) Designed flapping angle and (b) flapping mechanism after assembling parts made of 0.8-mm-thick glass/epoxy panels.

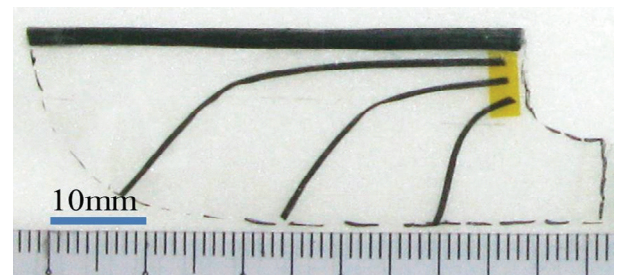


Fig. 3 Artificial wing with veins made of carbon/epoxy strips and membrane made of 20- μm -thin polyethylene terephthalate (PET).

along the trailing-edge connector at different distances from the reference location. When the wing root is placed at these holes, the wing becomes loose and passively generates wing twist during flapping motion. Thus, in this work, the wing-root offset is defined as the distance from the reference location to a hole location where the wing root is constrained. To investigate the effect of the wing-root offset on the aerodynamic force generation, we tested five cases of wing-root offsets

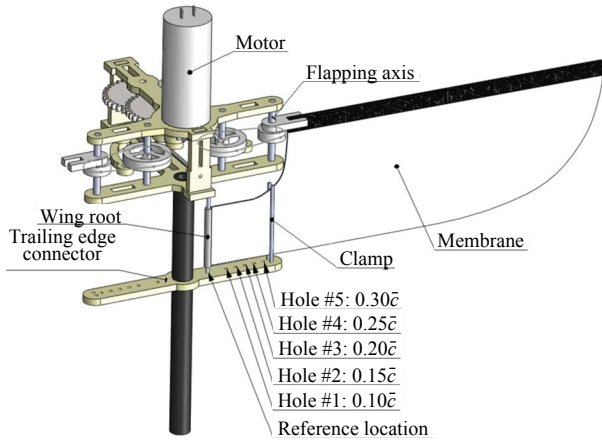


Fig. 4 Design of wing-root offset in right wing. The wing-root offset is defined as the distance from the reference position to a hole position where the wing root is constrained.

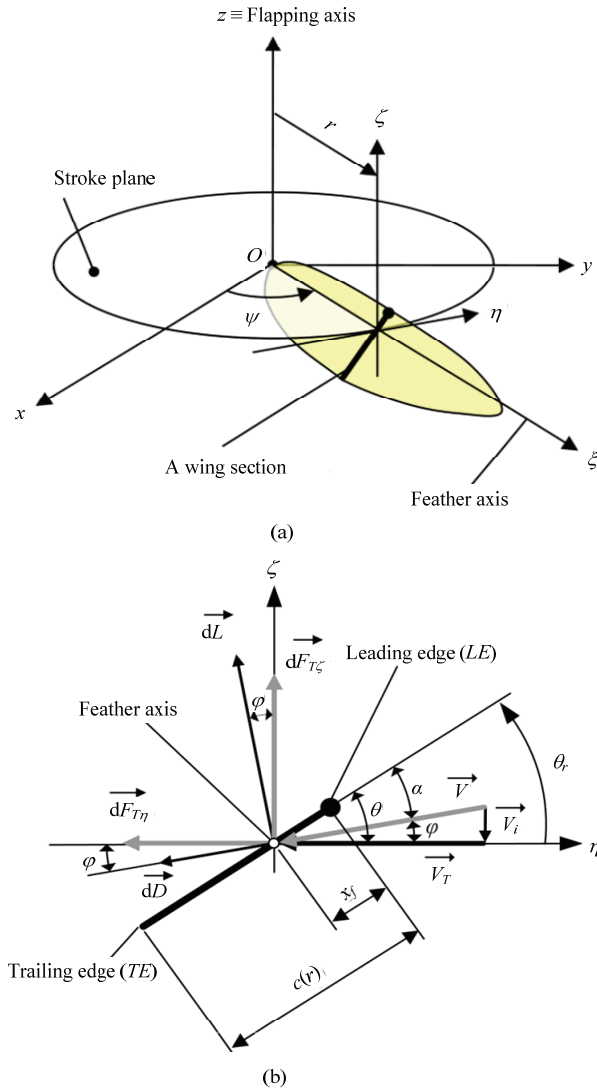


Fig. 5 (a) Definitions of wing section and (b) force components for UBET analysis^[32].

corresponding to the five hole locations in the trailing-edge connector shown in Fig. 4. The distances from the reference location to the holes ranged from 10% to 30% of the mean chord (\bar{c}) of the wing in $0.05\bar{c}$ increments. Hereafter in the paper, these offsets are denoted as $0.10\bar{c}$, $0.15\bar{c}$, $0.20\bar{c}$, $0.25\bar{c}$, and $0.30\bar{c}$, respectively. A clamp was installed along the flapping axis to generate passive camber from the clamp to the wing tip.

3 Estimation of thrust using UBET

The UBET, which employs full 3D wing kinematics, was proved to provide a reasonable estimation of aerodynamic forces in a previous work^[32]. Therefore, we used this model to estimate the thrust produced by the FW-MAV in the present study. In the UBET, the wing is divided into many finite wing sections or blade elements. The force acting in each wing section is distributed into four force components: translational force, added mass force, rotational force, and inertial force^[32,33]. Further details of calculation of each force component can be found elsewhere^[32].

The motion of a flapping wing is the combination of two actions: flapping around the flapping axis (z -axis) and rotation around the feather axis (ζ -axis in Fig. 5a). The feather axis is attached to the leading edge of the wing and flaps in the xy plane or stroke plane. The location of the feather axis is determined by the flapping angle ψ , as shown in Fig. 5a. The rotation angle of each wing section at a distance r from the flapping axis or wing root, which is denoted by θ_r , is defined as the angle between the η -axis and the wing section, as shown in Fig. 5b. The FW-MAV is designed to flap its wings symmetrically on the stroke plane about the plane of symmetry, which is the yz plane. Consequently, the force generated by the two wings in the x direction is canceled out, and therefore, the force components in only the y and z directions were considered in the present calculation.

The translational force in the y direction, $dF_{Ty}(t)$, and that in the z direction, $dF_{Tz}(t)$, at a time instant t are determined as

$$dF_{Ty}(t) = (-dL \sin \varphi - dD \cos \varphi) \cos \psi, \quad (9)$$

$$dF_{Tz}(t) = dL \cos \varphi - dD \sin \varphi, \quad (10)$$

where $dL = \frac{1}{2} \rho C_L V^2 dS$ and $dD = \frac{1}{2} \rho C_D V^2 dS$. The

variables ρ , dS , V , and φ denote the air density, wing section area, inflow velocity, and induced angle, respectively. Further, C_L and C_D denote the lift and drag coefficients, respectively, whose values were acquired from a previous experiment^[8]. The two coefficients were verified to be applicable for a Reynolds number on the order of 10^4 in an earlier work^[32].

The added masses acting on a wing section in the y and z directions are calculated as

$$dF_{Ay}(t) = \frac{\pi}{4} \rho c^2 a_n \sin \theta_r \cos \psi dr, \quad (11)$$

$$dF_{Az}(t) = -\frac{\pi}{4} \rho c^2 a_n \cos \theta_r dr, \quad (12)$$

where c is the wing chord length;

$$a_n = r\ddot{\psi} \sin \theta_r + (c/2 - x_f)\ddot{\psi}^2 \cos \theta_r \sin \theta_r + (c/2 - x_f)\ddot{\theta}_r,$$

which denotes the acceleration of the center of the wing section at a time instant; and x_f is the distance between the feather axis and the leading edge on a wing section^[32].

The third aerodynamic force component—rotational force—acts normally to the surface of the wing section^[33]. The amplitude of the rotational force acting on a wing section is determined by

$$dF_{rot} = \rho V_T c_{rot} \dot{\theta}_r c^2 dr, \quad (13)$$

where V_T is the translational velocity, $\dot{\theta}_r$ is the rotational velocity, and c_{rot} is rotational force coefficient and is a function of non-dimensional rotational velocity and the position x_f of the feather axis.

Eq. (13) can be decomposed into components in the y and z directions at a time instant t as

$$dF_{Ry}(t) = -dF_{rot} \sin \theta_r \cos \psi, \quad (14)$$

$$dF_{Rz}(t) = dF_{rot} \cos \theta_r. \quad (15)$$

In addition to the abovementioned three aerodynamic force components, the inertial force of the wing is also included in the UBET model. Its components in the y and z directions are expressed as

$$dF_{Iy}(t) = \int_{TE}^{LE} (dm_w) \ddot{y}, \quad (16)$$

$$dF_{Iz}(t) = \int_{TE}^{LE} (dm_w) \ddot{z}, \quad (17)$$

where dm_w is the mass of a wing section in the chordwise direction and \ddot{y} and \ddot{z} are the accelerations of the mass dm_w at a time instant in the y and z directions, respectively^[32,33].

Eventually, the forces generated by the two wings in the y and z directions can be obtained by integrating the summation of the force components produced by all the wing sections over the wing length R as

$$F_y(t) = 2 \int_0^R (dF_{Ty} + dF_{Ay} + dF_{Ry} + dF_{Iy}), \quad (18)$$

$$F_z(t) = 2 \int_0^R (dF_{Tz} + dF_{Az} + dF_{Rz} + dF_{Iz}). \quad (19)$$

The average forces in the y and z directions over a flapping cycle can be calculated as

$$F_{y,ave} = \frac{1}{T} \int_0^T F_y(t) dt, \quad (20)$$

$$F_{z,ave} = \frac{1}{T} \int_0^T F_z(t) dt, \quad (21)$$

where T is the flapping period of the wings. $F_{y,ave}$ and $F_{z,ave}$ are hereafter referred to as the “mean horizontal force” and “mean vertical force” or “mean thrust”, respectively.

4 Experimental test setup for wing kinematics and force generation

4.1 Wing kinematics measurement

To measure the wing kinematics, markers were attached on the leading edge and trailing edge of the wings at three wing sections—0.25, 0.50, and 0.75—along the wingspan (R). A calibration cube was used to calibrate the measurement system based on the coordinates of predetermined marked points on the cube. The location of the marked points at the wing sections during the flapping motion was tracked using three high-speed cameras synchronized at 2000 fps. The sequential images obtained from these cameras were analyzed by the Direct Linear Transformation (DLT) method developed by Hedrick^[34] in MATLAB code. Details of measurement of the wing kinematics can be found elsewhere^[20,32].

From the acquired images, the time histories of the flapping angle and rotation angle were obtained on the basis of the coordinates of the marked points at the three wing sections during flapping motions. Summation of

sine and cosine functions was used as a fitting function to fit the measured time histories of the two angles based on the least-squares method^[35,36]. The form of the fitting function is expressed as

$$\kappa(t) = a_0 + \sum_{k=1}^3 [a_k \cos(2k\pi ft) + b_k \sin(2k\pi ft)], \quad (22)$$

where $\kappa(t)$ is either the flapping angle or the rotation angle at a time instant t ; f is the flapping frequency; and a_0 , a_k , and b_k ($k = 1, 2, 3$) are the coefficients specified according to the least-squares method.

The fitting function for the flapping angle and rotation angle was subsequently input to the UBET to estimate the forces generated by the flapping wing. From the wing rotation angles measured at the three wing sections of $0.25R$, $0.5R$, and $0.75R$, we can perform interpolation and extrapolation to obtain the wing rotation angle at an arbitrary wing section along the wing-span.

4.2 Force and power measurements

The forces generated by the flapping wing were measured using a multi-axis load cell (Nano 17, Stainless steel, ATI Industrial Automation, USA, force resolution of 0.3 gf). The load cell was installed vertically in the flapping-wing system through an adapter made of a carbon rod with a diameter of 7 mm, as shown in Fig. 6a. The force signal from the load cell was transmitted to a computer and recorded by ATI DAQ F/T software (ATI Industrial Automation, Version 1.0.4.2.2). The flapping-wing system was excited by an external power supply (E3646A, Agilent, Malaysia) at flapping frequencies in the range of 26 Hz – 36 Hz with increments of 2 Hz for each wing-root offset.

The typical time history of the vertical force measured by the load cell when the wings were excited at 26 Hz is shown in Fig. 6b. Right before and after exciting the wings for about 100 flapping cycles, the load cell was activated under idle conditions for reference in order to calculate the average value of the measured forces. The average forces were calculated from about 80 continuous cycles after excluding the cycles close to the transition stages between the idle conditions and the force signal. More than 10 experimental tests were conducted for each wing-root offset at the same flapping frequency. To acquire the time history

of the measured force, a low-pass filter with a cutoff frequency three times the flapping frequency was used to eliminate the high-frequency signals in the measured data.

During force measurement, input power applied to the flapping-wing system was also measured in each case by using an oscilloscope (TDS 2024, Tektronix Inc.) and a resistance. Fig. 7 shows the experimental test setup for power measurement. The power was calculated by integrating the product of the instant input voltage to the motor and the instant current over a time period as expressed below:

$$P_i = \frac{1}{T} \int_0^T V_M(t) I(t) dt, \quad (23)$$

where P_i is the input power applied to the flapping-wing system; T is the time period; V_S and V_M are the output

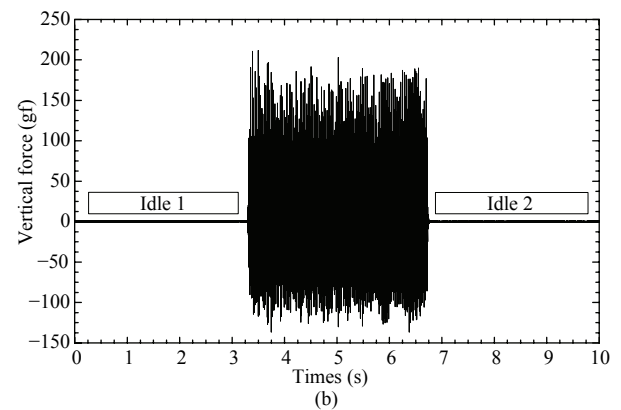
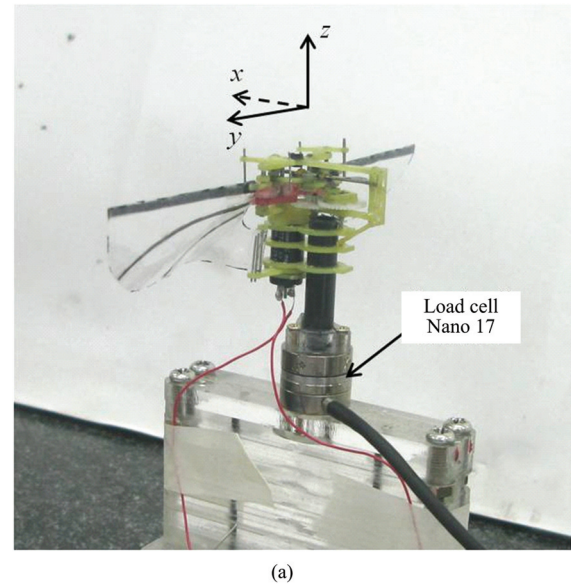


Fig. 6 (a) Experimental setup for force measurement and (b) definition of one batch dataset from raw vertical force data recorded by the measurement system when the flapping-wing system was operated at 26 Hz.

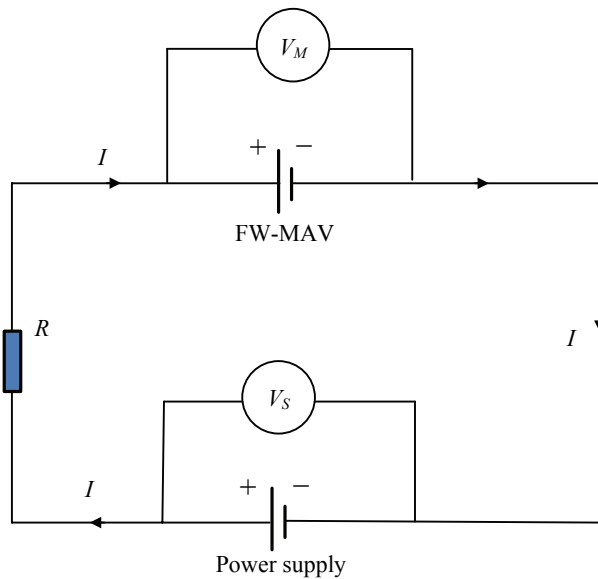


Fig.7 Power consumption measurement.

voltage of the power supply and input voltage to the flapping-wing system, respectively; R is the resistance; and $I(t) = (V_S(t) - V_M(t))/R$ is the instant current applied to the flapping-wing system.

5 Results and discussion

5.1 Wing kinematics

The developed flapping-wing system creates passive wing rotation and wing twist. Therefore, adjustment of the wing-root offset is expected to produce a proportional amount of offset in the wing rotation angles. To confirm this hypothesis, the wing kinematics were measured for three wing-root offsets: $0.15\bar{c}$, $0.20\bar{c}$, and $0.25\bar{c}$. The wing kinematics for the wing-root offsets of $0.10\bar{c}$ and $0.30\bar{c}$ were extrapolated from the measured ones by the linear extrapolation technique^[37].

Fig. 8 shows the measured wing kinematics after curve fitting for the three wing-root offsets. Since the flapping-wing system was designed to flap its wings at the same flapping angle for all wing-root offsets, the time histories of the flapping angles are similar for the three offsets, as shown in Fig. 8a. The amplitudes of the flapping angles were approximately 180° . This angle is similar to the flapping angle of a real beetle's hind wing during hovering^[32] and slightly larger than the designed flapping angle of 170° . The time histories of the wing rotation angles for the three offsets at three locations corresponding to 25%, 50%, and 75% wingspan are

plotted in Figs. 8b–8d, respectively. It is clear from the figures that the wing rotation angle is significantly affected by a change in the wing-root offset. It should be noted that the amplitude of the wing rotation angle increases with the offset at the wing root.

Before using the measured wing kinematics to linearly extrapolate the wing kinematics for two additional wing-root offsets of $0.10\bar{c}$ and $0.30\bar{c}$, we verified the extrapolation technique to prove that linear extrapolation can provide reasonably accurate wing kinematics. To this end, wing kinematics for the wing-root offsets of $0.15\bar{c}$ and $0.25\bar{c}$ were obtained by extrapolating the wing kinematics measured for the other wing-root offsets. The wing kinematics at the offset of $0.15\bar{c}$ was linearly extrapolated from those for the wing-root offsets of $0.20\bar{c}$ and $0.25\bar{c}$. Likewise, the wing kinematics of the offset of $0.25\bar{c}$ was confirmed by the linear extrapolation from the fitted wing rotation angles of the wing-root offsets of $0.15\bar{c}$ and $0.20\bar{c}$. The extrapolated wing kinematics were then compared with those measured for the offsets of $0.15\bar{c}$ and $0.25\bar{c}$ by applying them to the UBET for force estimation. We could confirm that the extrapolated wing kinematics for the wing-root offset of $0.15\bar{c}$ and $0.25\bar{c}$ were in good agreement with the measured ones, respectively.

Afterward, the linear extrapolation technique was applied to the estimation of the wing rotations for the wing-root offsets of $0.10\bar{c}$ and $0.30\bar{c}$ by using the wing kinematics measured for the wing-root offsets of $0.15\bar{c}$, $0.20\bar{c}$, and $0.25\bar{c}$. The results are plotted in Fig. 8 along with the wing kinematics for the wing-root offsets of $0.15\bar{c}$, $0.20\bar{c}$, and $0.25\bar{c}$ at three different locations in the spanwise direction. Since the time history of the flapping angle was not too strongly affected by the wing-root offsets, the time histories of flapping angles for the extrapolated wing kinematics were calculated by taking the average of the measured flapping angles, as shown in Fig. 8a. Subsequently, these wing kinematics were employed for thrust estimation by the UBET as described in the next section.

5.2 Generated vertical and horizontal forces

The time histories of mean forces for the five wing-root offsets measured experimentally and estimated theoretically by the UBET at a flapping frequency

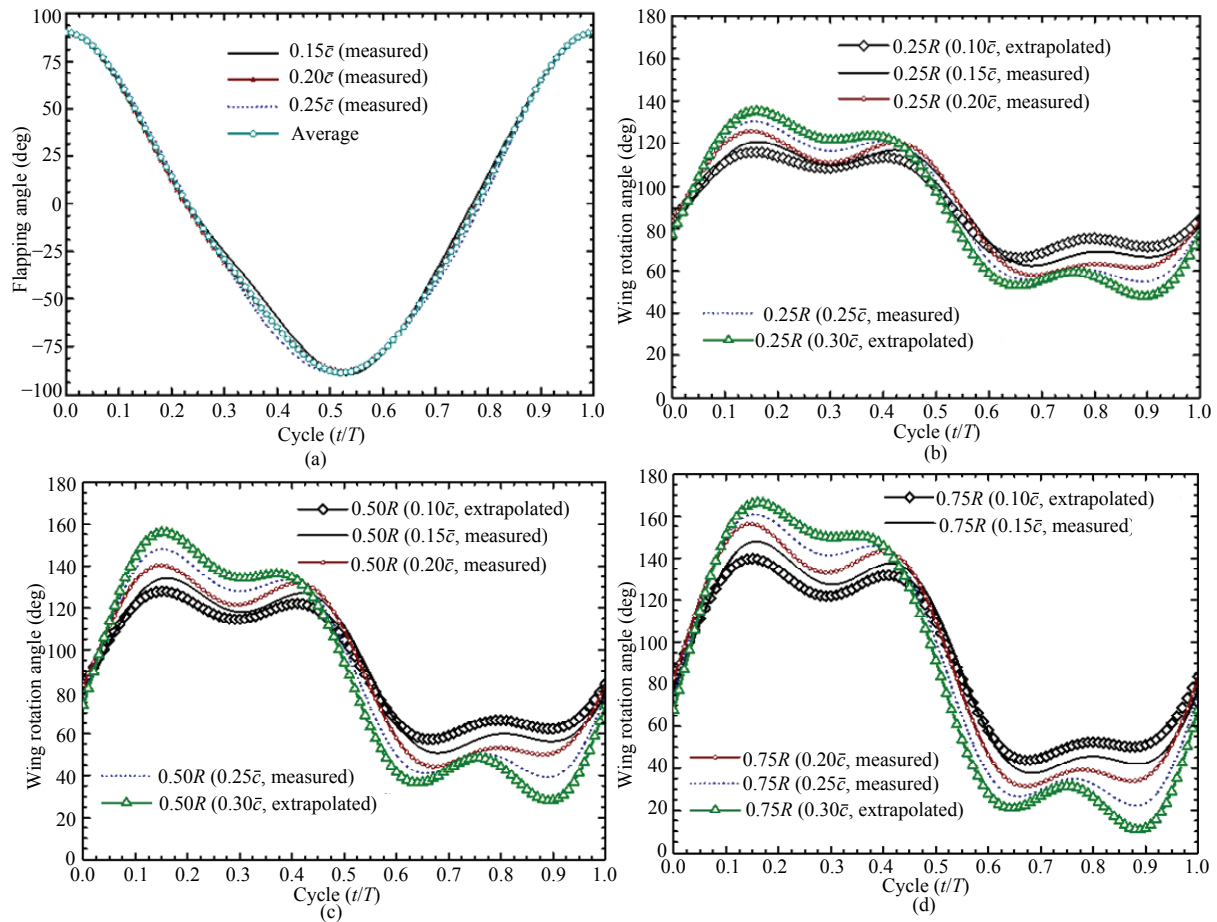


Fig. 8 Wing kinematics at flapping frequency of 26 Hz in the developed flapping-wing system with various wing-root offsets. (a) Flapping angle, (b) wing rotation angle at 25% wingspan, (c) wing rotation angle at 50% wingspan, and (d) wing rotation angle at 75% wingspan.

of 26 Hz are displayed in Fig. 9 and Table 1, respectively. In Fig. 9, the vertical forces are represented by the solid lines with symbols, whereas the horizontal forces are represented by the solid, dashed, and dotted lines without symbols. Different colors denote different methods used to acquire the time histories: blue indicates the measured data, black indicates data obtained by UBET estimation performed using the measured wing kinematics, and red indicates data obtained by UBET estimation performed using the extrapolated wing kinematics. Despite some differences, the time histories of the estimated vertical and horizontal forces show similar tendencies to those of the measured vertical and horizontal forces. The measured mean vertical forces are typically up to 8% larger than the corresponding estimated values. The differences are reasonable considering that the flapping wings create curved cross sections during flapping motion, which contributes to the generation of larger aerodynamic forces than those pro-

duced by flat sections used in the UBET analysis^[19]. The averages of the vertical forces estimated using the measured wing kinematics are in good agreement with those obtained using the extrapolated wing kinematics. The differences are 2.3% and 1.4% for the offsets of $0.15\bar{c}$ and $0.25\bar{c}$, respectively. Therefore, we expect that the extrapolated wing kinematics for the offsets of $0.10\bar{c}$ and $0.30\bar{c}$ can be applied to the UBET for calculating the corresponding forces with reasonable accuracy. As a result, the vertical forces estimated based on the extrapolated wing kinematics are in good agreement with the measured vertical forces for both wing-root offsets of $0.10\bar{c}$ and $0.30\bar{c}$, for which the differences are 7.1% and 1.5%, respectively. As shown in Fig. 9, most of the average horizontal forces are only about 5% of the vertical forces in both the estimations and the measurements. These results are reasonable because the wing motion is approximately symmetric during the downstroke and upstroke.

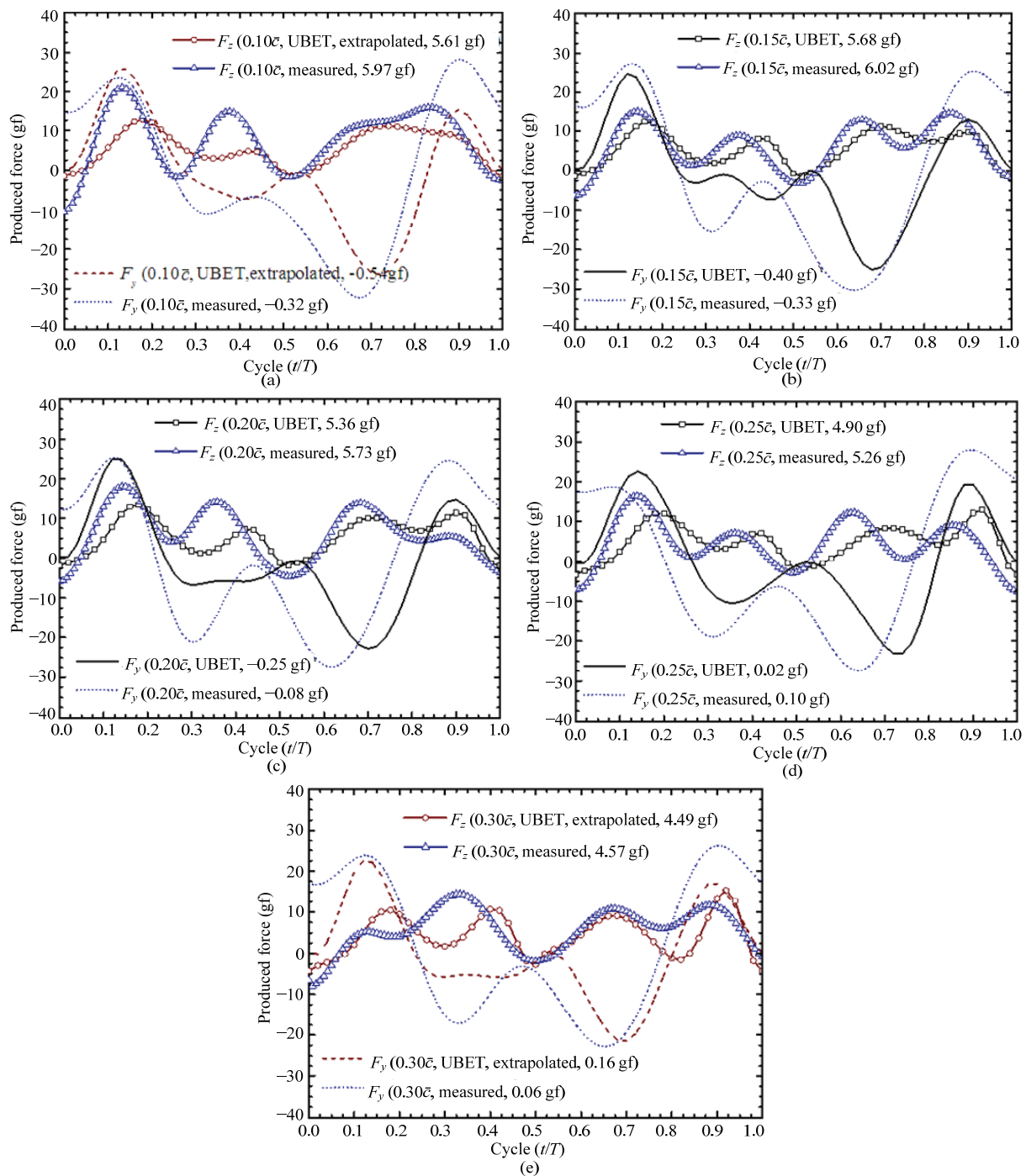


Fig. 9 Comparison of time histories of vertical and horizontal forces obtained from load-cell measurement with those obtained by UBET estimation (using both the measured and the extrapolated wing kinematics) in a cycle for wing-root offsets of (a) $0.10 \bar{c}$, (b) $0.15 \bar{c}$, (c) $0.20 \bar{c}$, (d) $0.25 \bar{c}$, and (e) $0.30 \bar{c}$.

The results in Table 1 indicate that flapping wings with wing-root offsets of $0.10 \bar{c}$ and $0.15 \bar{c}$ generate larger vertical forces than those with the other wing-root offsets at a flapping frequency of 26 Hz. To prove this claim for other flapping frequencies, the vertical forces and power consumptions during flapping motion were

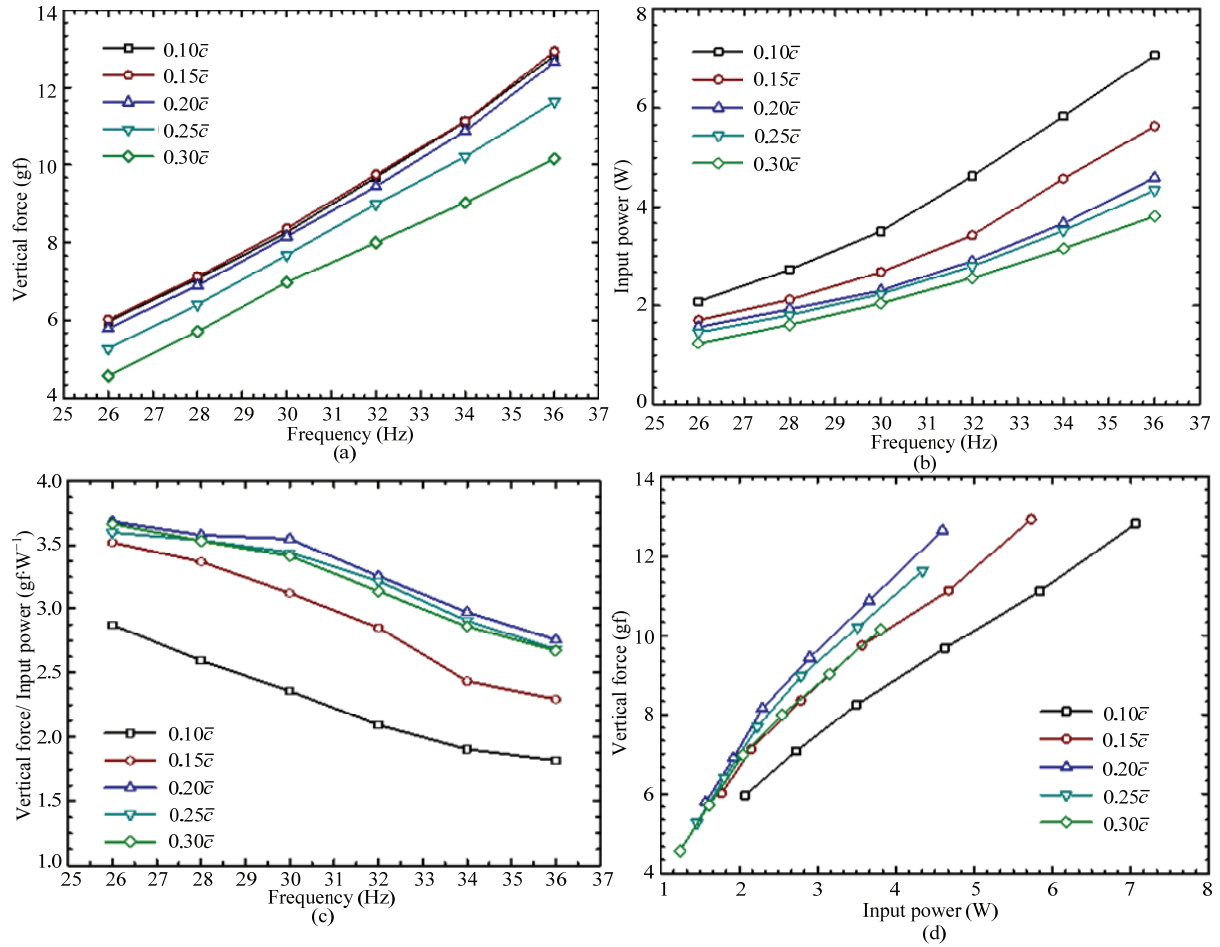
measured for all wing-root offsets at various flapping frequencies, as shown in Fig. 10. Fig. 10a confirms that the wing-root offsets of $0.10 \bar{c}$ and $0.15 \bar{c}$ showed the largest vertical forces or thrusts. However, in terms of the force-to-input-power ratio shown in Fig. 10c, it is not the case. Indeed, Fig. 10b shows that the flapping-wing

Table 1 Comparison of vertical forces obtained by different methods at various wing-root offsets

Wing-root offsets	Measurement (gf and STD*)	UBET (Measured wing kinematics)	UBET (Extrapolated wing kinematics) (gf)	Difference (%)
$0.10\bar{c}$	5.97 ± 0.17	N/A	5.61	6.0
$0.15\bar{c}$	6.02 ± 0.14	5.68	5.55	5.6 (2.3)**
$0.20\bar{c}$	5.79 ± 0.16	5.36	N/A	7.4
$0.25\bar{c}$	5.26 ± 0.13	4.90	4.97	6.8 (-1.4)**
$0.30\bar{c}$	4.57 ± 0.16	N/A	4.49	1.8

* STD = Standard deviation

** Difference between the estimated forces by the UBET based on the measured and extrapolated wing kinematics.

**Fig. 10** Measured vertical forces produced by the flapping-wing system at various flapping frequencies. (a) Average vertical force, (b) input power, (c) force-to-input-power ratio and, (d) vertical force vs. input power.

system using the wings with these offsets consumed more power to flap the wings than that with other offsets. We can see that the wing with the wing-root offset of $0.20\bar{c}$ produced the highest force-to-input-power ratio, as indicated in Fig. 10c. Further, as shown in Fig. 10a, the vertical force produced by the offset of $0.20\bar{c}$ was only about 4% less and the corresponding force-to-input-power ratio was about 30% and 10% higher than those for the offsets of $0.10\bar{c}$ and $0.15\bar{c}$, respectively. In addition, the force-to-input-power ratio

indeed plays an important role in and is a key consideration for developing a FW-MAV^[38,39]. As a result, the wing with the wing-root offset of $0.20\bar{c}$ can be regarded as an optimal configuration for achieving high thrust and less power consumption of our hovering FW-MAV. Fig. 10d shows that the vertical force is affected mainly by the power applied to the system. When the same wing configurations and wing kinematics are used, a higher input power obviously produces a larger vertical force in the hovering FW-MAV.

5.3 Distribution of force components

In this work, we consider the effect of the wing kinematics modulation on the generation of only vertical forces, since the horizontal force makes a very small contribution to our flapping-wing model during the flapping motion. In the UBET, the vertical force acting on a wing is a summation of four components: the translational force, added mass force, rotational force, and inertial force^[32]. The work of Truong *et al.*^[32] indicated that even though the inertial force affected the time history of the estimated force significantly, its contribution to the resultant force was negligible. Meanwhile, the translational force is a dominant component among the four force components. The distributions of the translational force, added mass force, rotational force, and resultant vertical force along a wingspan (R) are plotted in Fig. 11. For all cases, larger translational force is produced in the outer half of the wing because of the faster translational speed. As shown in Fig. 11a, the

translational forces (F_{Tz}) are inversely proportional to the values of the wing-root offsets. This means that the flapping wing with the wing-root offset of $0.10\bar{c}$ produces the largest translational force among the wings with the five offset values. Because the translational force is determined mainly by the effective AoA, the comparison among the results for the five wing-root offset cases can be explained reasonably by analyzing the effective AoA at each wing section along the wingspan.

In the present UBET model, the unsteady lift and drag coefficients measured by Dickinson *et al.*^[8] were used, which were previously proved to be applicable even in cases with relatively higher Reynolds numbers^[32]. As presented in the study of Dickinson *et al.*^[8], the lift coefficient is the highest at an AoA of about 45° and the drag coefficient increases with AoA, as shown in Fig. 12. Therefore, the largest vertical translational force can be generated by the wing-root offset case that

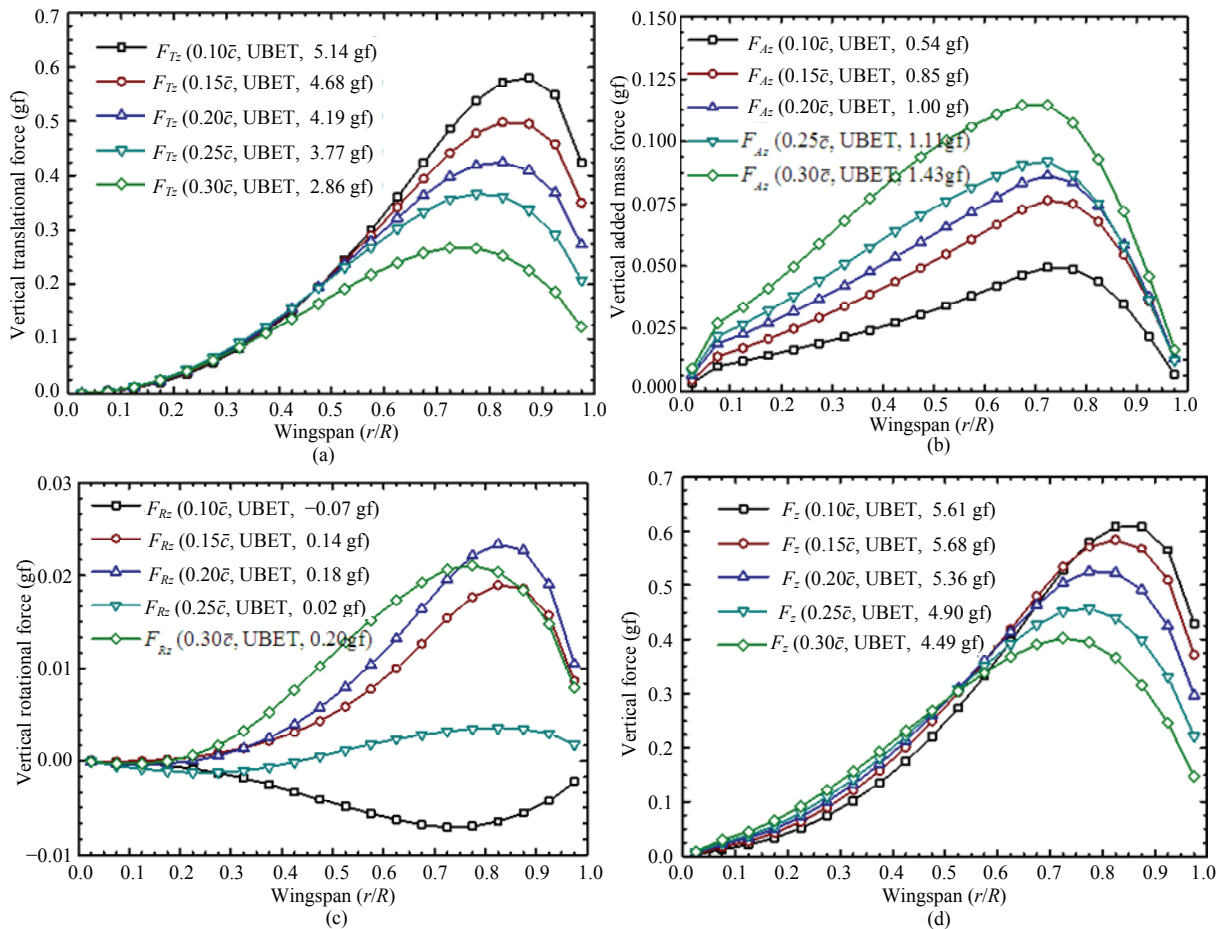


Fig. 11 Average of forces generated by each wing section over a flapping cycle along the wingspan with various wing-root offsets. (a) Translational force, (b) added mass force, (c) rotational force, and (d) resultant vertical forces. The translational and added mass forces contribute to a large amount of vertical forces in the flapping-wing system during the flapping motion.

generates an effective AoA close to 45° . The time histories of the effective AoAs at four locations along the wingspan ($0.2R$, $0.4R$, $0.6R$, and $0.8R$) are shown in Fig. 13. It is clear that the effective AoAs for the wing-root offset of $0.10\bar{c}$ are closer to the angle of the maximum lift coefficient (45°) at all locations in the outer half of the wing (60% and 80% wingspans in Figs. 13c and 13d, respectively). This explains why the largest translational force is generated at this wing-root offset.

The results in Fig. 11b indicate that not only the translational force but also the added mass force makes an important contribution to the resultant force. Contrary to the translational force, the added mass force (F_{Az}) increases proportionally with wing-root offset. This result is reasonable because the added mass force in the z -direction includes the cosine function of the rotation angle, as indicated in Eq. (12). The rotational forces (F_{Rz}) along the wingspan in Fig. 11c are negligible in our flapping-wing system since their contribution to the net forces is less than 5%.

On the basis of the obtained results, we can modify the wing rotation angle or AoA to improve the translational force for optimal generation of vertical forces in the hovering FW-MAV. However, changing the wing rotation angle may cause variation in the added mass

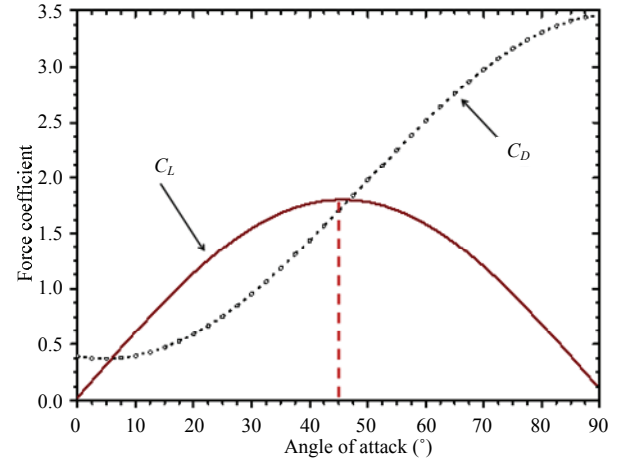


Fig. 12 Lift and drag coefficients obtained from study of Dickinson *et al.*^[8].

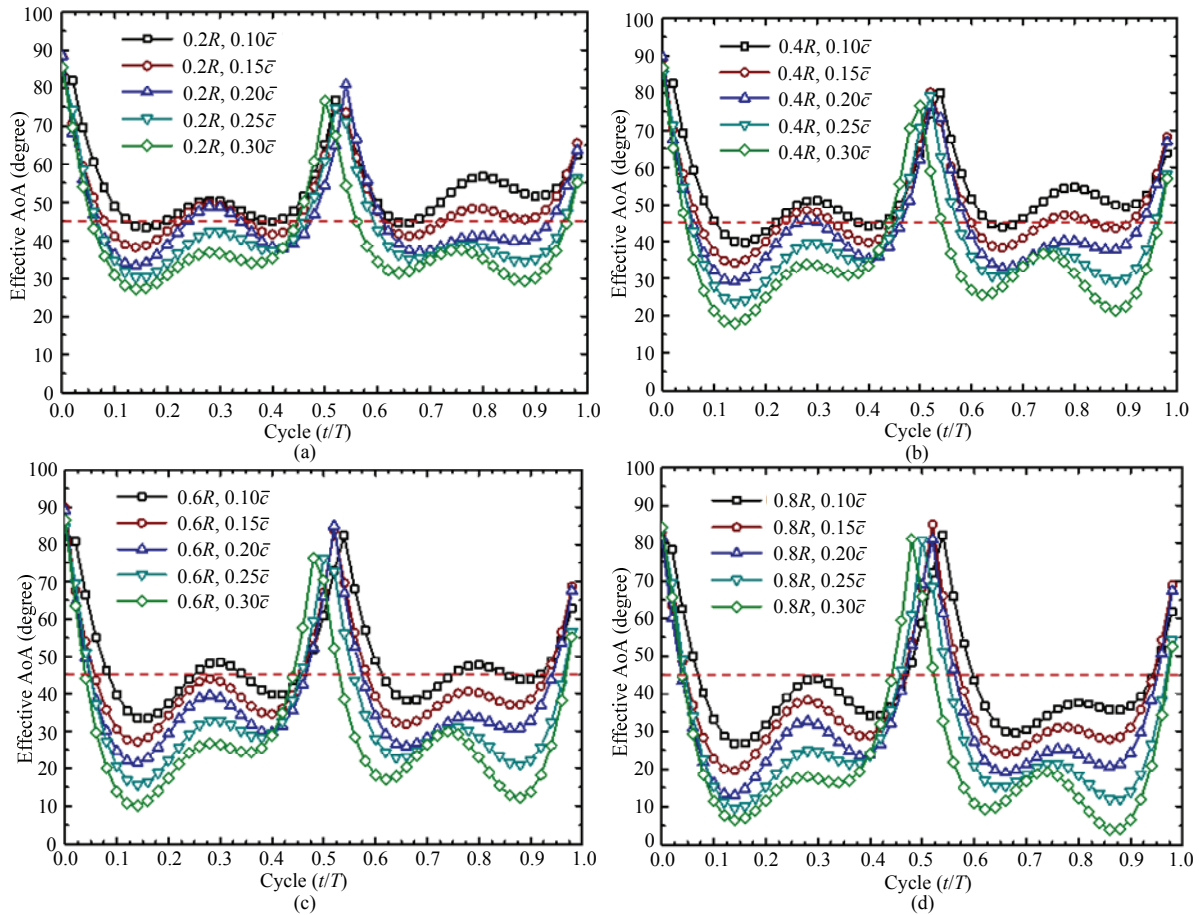


Fig. 13 Effective AoA at wing sections of 20%, 40%, 60%, and 80% wingspan. The dashed straight line represents the effective AoA for maximum lift at 45° .

force, which has a significant contribution to the resultant force. Therefore, finding an optimal wing rotation angle for generation of the largest force in a hovering FW-MAV remains a challenge.

Although wings with wing-root offsets of $0.10\bar{c}$ and $0.15\bar{c}$ produce the highest thrusts, the wing-root offset of $0.20\bar{c}$ is the most optimal in terms of efficiency based on the thrust-to-input-power ratio as shown in Fig. 10c. From the lift and drag coefficient values obtained from Dickinson *et al.*^[8], wings with the wing-root offset that creates a high effective AoA also produce high drag, as shown in Fig. 12. Consequently, at this wing-root offset, the system needs higher power to flap its wings at the same flapping frequencies in comparison to that in other cases of wing-root offsets (Fig. 10b).

This result can partially explain how flying insects vary their wing kinematics to generate useful aerodynamic forces for different flight modes. Insects use the muscles attached at the wing base to actively generate the flapping angle as well as the wing rotation angle for their flight performance^[30]. Bahlman *et al.*^[40] conducted a study using a robotic bat wing and also found that flight can be implemented either at the cost of a large amount of energy when thrust is necessary or with a smaller energy requirement when thrust is not of much significance. Thus, depending on their body weight and flight conditions, insects can adjust their wings using appropriate wing kinematics to produce enough force to lift them upward for saving energy during flight.

6 Conclusion

In this study, the effect of wing kinematics modulation on the generation of aerodynamic forces in a hovering FW-MAV was investigated by changing the wing-root offset. The time histories of the flapping angles were not affected by a change in the wing-root offsets; however, the time histories of the wing rotation angles at various offsets showed clear differences at the same wingspan locations. The extrapolated wing kinematics were found to be reasonable and acceptable on the basis of verification performed using the measured wing kinematics and generated thrusts. The differences between the thrusts estimated by the UBET using the extrapolated wing kinematics and the measured wing kinematics were about 2.3% and 1.4% for the wing-root

offsets of $0.15\bar{c}$ and $0.25\bar{c}$, respectively. The results obtained from experiment and estimation revealed that the FW-MAV using wings with wing-root offsets of $0.10\bar{c}$ and $0.15\bar{c}$ produced the highest thrusts, whereas that with the wing-root offset of $0.20\bar{c}$ yielded the optimal thrust-to-input-power ratio. By analyzing the effective AoA and the force components, the results could be reasonably explained. Numerical study conducted with UBET method also demonstrated that the translational force and added mass force are dominant among four force components. Even though there was only one case of wing aspect ratio discussed here, this study is expected to provide useful information for developing hovering FW-MAVs.

Acknowledgment

This research was supported by a grant to the Bio-Mimetic Robot Research Center (UD130070ID) funded by the Defense Acquisition Program Administration and partially supported by the Basic Science Research Program through the National Research Foundation of Korea (NRF) funded by the Ministry of Science, ICT and Future Planning (Grant No. 2013R1A2A2A01067315).

References

- [1] Ma K Y, Chirarattananon P, Fuller S B, Wood R J. Controlled flight of a biologically inspired insect-scale robot. *Science*, 2013, **340**, 603–607.
- [2] Keennon M T, Klingebiel K, Won H, Andriukov A. Development of the nano hummingbird: A tailless flapping wing micro air vehicle. *Proceeding of 50th AIAA Aerospace Sciences Meeting*, Nashville, USA, 2012.
- [3] de Croon G C, Groen M A, De Wagter C, Remes B, Ruijsink R, van Oudheusden B W. Design, aerodynamics, and autonomy of the DelFly. *Bioinspiration and Biomimetics*, 2012, **7**, 025003.
- [4] Phan H V, Nguyen Q V, Truong Q T, Truong T V, Park H C, Byun D Y, Goo N S, Kim M J. Stable vertical takeoff of an insect-mimicking flapping-wing system without guide implementing inherent pitching stability. *Journal of Bionic Engineering*, 2012, **9**, 391–401.
- [5] Weis-Fogh T. Quick estimates of flight fitness in hovering animals, including novel mechanisms for lift production. *The Journal of Experimental Biology*, 1973, **59**, 169–230.
- [6] Dickinson M H, Gotz K G. Unsteady aerodynamic performance of model wings at low Reynolds numbers. *The*

- Journal of Experimental Biology*, 1993, **174**, 45–64.
- [7] Ellington C P, van den Berg C, Willmott A P, Thomas A L R. Leading-edge vortices in insect flight. *Nature*, 1996, **384**, 626–630.
- [8] Dickinson M H, Lehmann F, Sane S P. Wing rotation and the aerodynamic basis of insect flight. *Science*, 1999, **284**, 1954–1960.
- [9] Sun M, Tang J. Unsteady aerodynamic force generation by a model fruit fly wing in flapping motion. *The Journal of Experimental Biology*, 2002, **205**, 55–70.
- [10] Sane S P. The aerodynamics of insect flight. *The Journal of Experimental Biology*, 2003, **206**, 4191–4208.
- [11] Walker S M, Thomas A L R, Taylor G K. Deformable wing kinematics in free-flying hoverflies. *Journal of the Royal Society Interface*, 2010, **7**, 131–142.
- [12] Le T Q, Truong T V, Park S H, Truong T Q, Ko J H, Park H C, Byun D. Improvement of the aerodynamic performance by wing flexibility and elytra-hind wing interaction of a beetle during forward flight. *Journal of the Royal Society Interface*, 2013, **10**, 20130312.
- [13] Truong T V, Le T Q, Byun D, Park H C, Kim M. Flexible wing kinematics of a free-flying beetle (*Rhinoceros beetle trypoxylus dichotomus*). *Journal of Bionic Engineering*, 2012, **9**, 177–184.
- [14] Le T Q, Truong T V, Tran H T, Park S H, Ko J H, Park H C, Yoon K J, Byun D. Two- and three-dimensional simulations of beetle hind wing flapping during free forward flight. *Journal of Bionic Engineering*, 2013, **10**, 316–328.
- [15] Zeng L, Hao Q, Kawachi K. A scanning projected line method for measuring a beating bumblebee wing. *Optics Communications*, 2000, **183**, 37–43.
- [16] Nakata T, Liu H. Aerodynamic performance of a hovering hawkmoth with flexible wing: A computational approach. *Proceedings of the Royal Society B*, 2012, **279**, 722–731.
- [17] Walker S M, Thomas A L R, Taylor G K. Deformable wing kinematics in desert locust: How and why do camber, twist and topography vary through the stroke?. *Journal of the Royal Society Interface*, 2009, **6**, 735–747.
- [18] Young J, Walker S M, Bomphrey R J, Taylor G K, Thomas A L R. Details of insect wing design and deformation enhance aerodynamic function and flight efficiency. *Science*, 2009, **325**, 1549–1552.
- [19] Du G, Sun M. Effects of wing deformation on aerodynamic forces in hovering hoverflies. *The Journal of Experimental Biology*, 2010, **213**, 2273–2283.
- [20] Truong T Q, Phan V H, Park H C, Ko J H. Effect of wing twisting on aerodynamic performance of flapping wing system. *AIAA Journal*, 2013, **51**, 1612–1620.
- [21] Karasek M, Preumont A. Flapping flight stability in hover: A comparison of various aerodynamic models. *International Journal of Micro Air Vehicles*, 2012, **4**, 203–226.
- [22] Chan W L, Nguyen Q V, Debiassi M. Pitch and yaw control of tailless flapping wing MAVs by implementing wing root angle deflection. *International Micro Air Vehicle Conference and Competition*, Delft, The Netherlands, 2014.
- [23] Phan H V, Truong Q T, Park H C. Implementation of initial passive stability in insect-mimicking flapping-wing micro air vehicle. *International Journal of Intelligent Unmanned Systems*, 2015, **3**, 18–38.
- [24] Ansari S A, Knowles K, Zbikowski R. Insectlike flapping wings in the hover Part 1: Effect of wing kinematics. *Journal of Aircraft*, 2008, **45**, 1945–1954.
- [25] Altshuler D L, Dudley R. Kinematics of hovering hummingbird flight along simulated and natural elevational gradients. *The Journal of Experimental Biology*, 2003, **206**, 3139–3147.
- [26] Chai P, Chen J S, Dudley R. Transient hovering performance of hummingbirds under conditions of maximal loading. *The Journal of Experimental Biology*, 1997, **200**, 921–929.
- [27] Wu J H, Sun M. Unsteady aerodynamic forces of a flapping wing. *The Journal of Experimental Biology*, 2004, **207**, 1137–1150.
- [28] Sane S P, Dickinson M H. The control of flight force by a flapping wing: Lift and drag production. *The Journal of Experimental Biology*, 2001, **204**, 2607–2626.
- [29] Usherwood J R, Ellington C P. The aerodynamics of revolving wings. II. Propeller force coefficients from mayfly to quail. *The Journal of Experimental Biology*, 2002, **205**, 1565–1576.
- [30] Nguyen Q V, Park H C, Goo N S, Byun D. Characteristics of a beetle's free flight and a flapping wing system that mimics beetle flight. *Journal of Bionic Engineering*, 2010, **7**, 77–86.
- [31] Truong Q T, Phan H V, Sane S P, Park H C. Pitching moment generation in an insect-mimicking flapping-wing system. *Journal of Bionic Engineering*, 2014, **11**, 36–51.
- [32] Truong Q T, Nguyen Q V, Truong V T, Park H C, Byun D Y, Goo N S. A modified blade element theory for estimation of forces generated by a beetle-mimicking flapping wing system. *Bioinspiration and Biomimetics*, 2011, **6**, 036008.
- [33] Sane S P, Dickinson M H. The aerodynamic effects of wing rotation and a revised quasi-steady model of flapping flight. *The Journal of Experimental Biology*, 2002, **205**, 1087–1096.
- [34] Hedrick T. Software techniques for two- and three-dimensional kinematic measurements of biological and biomimetic systems. *Bioinspiration and Biomimetics*, 2008, **3**,

- 034001.
- [35] *Matlab® User's Guide*, MathWorks Inc, 2006.
- [36] Björck A. *Numerical Methods for Least Squares Problems*, SIAM, Philadelphia, USA, 1996.
- [37] Dahlquist G, Björck A. (translated by Anderson N) *Numerical Methods*, Prentice Hall, 1974.
- [38] Heathcote S, Martin D, Gursul I. Flexible flapping airfoil propulsion at zero freestream velocity. *AIAA Journal*, 2004, **42**, 2196–2204.
- [39] Mazaheri K, Ebrahimi A. Experimental investigation of the effect of chordwise flexibility on the aerodynamics of flapping wings in hovering flight. *Journal of Fluids and Structures*, 2010, **26**, 544–558.
- [40] Bahlman J W, Swartz S M, Breuer K S. How wing kinematics affect power requirements and aerodynamic force production in a robotic bat wing. *Bioinspiration and Biomimetics*, 2014, **9**, 025008.